




# Role of local temperature in the current-driven metal–insulator transition of $\text{Ca}_2\text{RuO}_4$

Giordano Mattoni <sup>1,\*</sup>, Shingo Yonezawa <sup>1</sup>, Fumihiko Nakamura,<sup>2</sup> and Yoshiteru Maeno <sup>1</sup>

<sup>1</sup>*Department of Physics, Graduate School of Science, Kyoto University, Kyoto 606-8502, Japan*

<sup>2</sup>*Department of Education and Creation Engineering, Kurume Institute of Technology, Fukuoka 830-0052, Japan*



(Received 10 July 2020; accepted 1 October 2020; published 17 November 2020)

It was recently reported that a continuous electric current is a powerful control parameter to trigger changes in the electronic structure and metal–insulator transitions (MITs) in  $\text{Ca}_2\text{RuO}_4$ . However, the spatial evolution of the MIT and the implications of the unavoidable Joule heating have not been clarified yet, often hindered by the difficulty to assess the local sample temperature. In this work, we perform infrared thermal imaging on single-crystal  $\text{Ca}_2\text{RuO}_4$  while controlling the MIT by electric current. The change in emissivity at the phase transition allows us to monitor the gradual formation and expansion of the metallic phase upon increasing current. Our local temperature measurements indicate that, within our experimental resolution, the MIT always occurs at the same local transition temperatures, irrespective of whether it is driven by temperature or current. Our results highlight the importance of local heating, phase coexistence, and microscale inhomogeneity when studying strongly correlated materials under the flow of electric current.

DOI: [10.1103/PhysRevMaterials.4.114414](https://doi.org/10.1103/PhysRevMaterials.4.114414)

## I. INTRODUCTION

In the field of quantum materials, extensive research interest has recently focused on strongly correlated systems, where unique changes of physical properties can be induced by external stimuli [1,2]. A paradigmatic example is the layered perovskite  $\text{Ca}_2\text{RuO}_4$ , a material having a Mott insulating ground state with antiferromagnetic ordering [3–5]. In this material, exotic phases presenting orbital ordering and unconventional magnetic modes have been reported [6,7]. Metallic states with paramagnetic, ferromagnetic, or superconducting character have been triggered by a series of control parameters, such as chemical composition [8,9], pressure [10–12], or strain [13–16].

More recently it was reported that a continuous electric current induces structural and electronic changes in  $\text{Ca}_2\text{RuO}_4$  [17,18]. Several subsequent works reported the emergence of novel phases in these nonequilibrium steady states induced by current [19–22]. An interesting development is the possibility of using a continuous current to trigger the material metal–insulator transition (MIT) [17], which naturally occurs at about 360 K in bulk single crystals [5]. In this framework, the coexistence of metallic and insulating regions stabilized by current has been reported by Zhang *et al.*, with a phase front characterized by nanoscale stripes of alternating phases [23].

However, the considerable amount of power supplied by a flowing current requires one to carefully take into account the unavoidable Joule heating, which makes it often difficult to measure the actual sample temperature. Recent reports by Fürsich *et al.* prove that heating by direct current can lead to a large temperature rise in  $\text{Ca}_2\text{RuO}_4$ , strongly depending on the

cooling technique [24]. Studies by Jenni *et al.* indicate that current-induced heating can lead to metal/insulator phase coexistence [25]. Moreover, Joule heating can cause less trivial effects in measurements. For example, current-induced diamagnetism reported by our group [26–29] was then revealed to be caused by localized heating of the sample holder [30]. Also, there are cases in which the occurrence of MITs in other materials has been linked to local heating effects [31–34]. Due to these considerations, a local temperature probe allowing direct imaging of  $\text{Ca}_2\text{RuO}_4$  is strongly desirable to uncover current-induced changes in the MIT.

Here, we study the current-driven MIT in  $\text{Ca}_2\text{RuO}_4$  by means of infrared (IR) thermal imaging. Our technique allows us to produce spatial maps of the local sample temperature, as well as to image the coexistence of metallic and insulating regions by making use of their different reflectivity. We uncover that the metallic phase forms and extends as a function of increasing continuous electrical current, and that a sample area becomes metallic or insulating whenever its local temperature crosses the characteristic MIT temperatures. Thus, within our experimental resolution, the value of these transition temperatures remains unchanged by the flowing current. Our imaging also allows us to reveal the formation of macroscopic cracks and defects during repeated cycles of current-driven MIT, which we find to strongly affect the MIT spatial evolution. These findings uncover the important role of local sample temperature in triggering phase transitions, in particular under the presence of direct current.

## II. RESULTS AND DISCUSSION

### A. Thermal imaging setup

For the experiment, we used the thermal imaging setup in Fig. 1(a). An IR camera (Avio, InfRec R500, spatial resolution

\*mattoni@scphys.kyoto-u.ac.jp

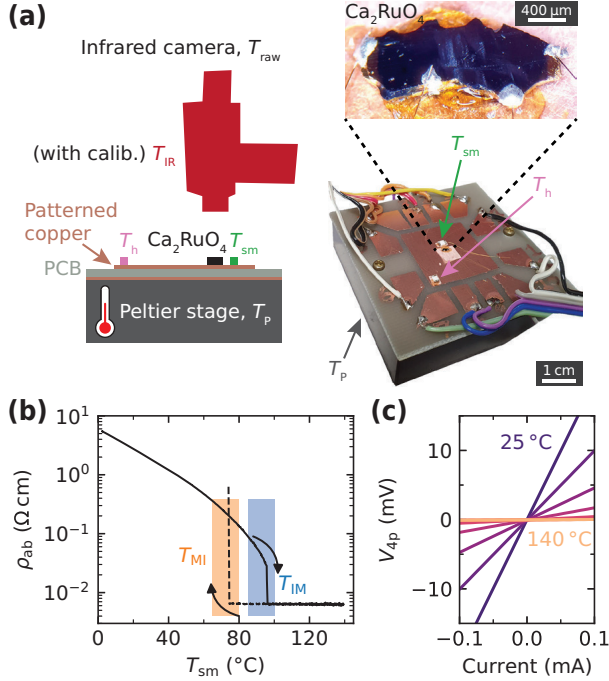


FIG. 1. Setup for thermal imaging. (a) Schematics and photographs of the thermal imaging setup, the sample holder, and a typical  $\text{Ca}_2\text{RuO}_4$  single crystal (sample no. 1) with electrical leads in a four-probe configuration. (b) Resistivity of  $\text{Ca}_2\text{RuO}_4$  as a function of  $T_{\text{sm}}$  controlled by varying the Peltier stage. The shaded regions show the range of temperatures where the insulator-to-metal ( $T_{\text{IM}}$ , blue) and metal-to-insulator ( $T_{\text{MI}}$ , orange) transitions are observed in our samples. Upon cooling (dashed line), a hysteresis is observed and the sample often breaks at  $T_{\text{MI}}$ . (c) Four-probe voltage-current characteristics in the low-current regime. A linear trend is observed at all temperatures, both in the insulating and in the metallic phases.

$21 \mu\text{m}$ , spectral range  $8\text{--}14 \mu\text{m}$ ) allows us to acquire optical maps of the raw IR reading  $T_{\text{raw}}$  that can be converted to the sample IR temperature  $T_{\text{IR}}$  upon calibration. A Peltier stage (Ampère, UT4070 with UTC-200A temperature controller) allows us to control the temperature of the thermal bath ( $T_{\text{p}}$ ) to which the sample is anchored. The sample holder consists of an FR-4 glass epoxy plate (Sunhayato, 31R, thickness  $1.6 \mu\text{m}$ ) covered on each face by a thin copper layer ( $35 \mu\text{m}$ ), which is patterned to provide contact pads on the top face. Two Pt1000 sensors (Heraeus, SMD 805-1000-B) are glued on the top copper layer with GE varnish in order to measure the temperature at a distance of  $1 \text{ mm}$  (sample monitor,  $T_{\text{sm}}$ ) and of  $15 \text{ mm}$  (holder,  $T_{\text{h}}$ ) from the sample. The copper layer enhances the thermal coupling between the sensors and the sample. We use high-purity  $\text{Ca}_2\text{RuO}_4$  single crystals of typical dimension between  $0.6 \times 0.5 \times 0.1$  and  $2 \times 1 \times 0.3 \text{ mm}^3$ , with an exposed  $a_0b_0$  surface in orthorhombic notation (see Fig. S1 in the supplemental material [35]). The sample is glued to the holder by using GE varnish with a layer of cigarette paper in between for electrical insulation. This configuration provides a strong thermal coupling, maximizing the cooling of the sample. To obtain low-resistance ohmic contacts, a thin layer of Au is sputtered at a  $45^\circ$  angle on the edges of the sample, and then connected to gold wires (thickness

$18 \mu\text{m}$ ) by using silver epoxy (Epotek, H20E). We measure a contact resistance smaller than  $100 \Omega$  at room temperature (Fig. S2 [35]). The electrical measurements are performed using a variable current source (Keysight, B2912A) and multimeters to measure the sample current and voltage (Keithley, 2000).

In Fig. 1(b), we show the typical resistivity of a  $\text{Ca}_2\text{RuO}_4$  sample measured in a four-probe configuration with constant current  $I = 10 \mu\text{A}$  (current density  $j \sim 0.01 \text{ A cm}^{-2}$ ). The sample temperature is measured by  $T_{\text{sm}}$  while varying the Peltier-stage temperature at  $1 \text{ K min}^{-1}$ . Upon warming, the resistivity shows the expected insulating trend, with a sharp drop at  $T_{\text{IM}}$ , where the sample becomes metallic. Upon cooling, the resistivity presents a clear hysteresis, consistent with previous results on  $\text{Ca}_2\text{RuO}_4$  [11,36], and typical of first-order phase transitions [37,38]. At  $T_{\text{MI}}$ , the sample turns back insulating, and we often lose the electrical contacts because the crystal shatters (vertical dashed line). The values of in-plane resistivity for the insulating ( $\rho_{\text{ab}} \sim 1 \Omega \text{ cm}$  at room temperature) and metallic ( $\rho_{\text{ab}} \sim 10^{-2} \Omega \text{ cm}$ ) phases indicate high-purity  $\text{Ca}_2\text{RuO}_4$  single crystals [5,8,39]. As shown in Fig. 1(c), the  $I$ - $V$  characteristics up to  $\pm 100 \mu\text{A}$  (current density  $\pm 0.1 \text{ A cm}^{-2}$ ) are linear, indicating that the sample is in an ohmic regime in the explored current range, both in the insulating and metallic phases.

The MIT of  $\text{Ca}_2\text{RuO}_4$  is rather abrupt and is known to involve a large change of the lattice parameters, with  $+1\%$  change of  $c_0$ , and up to  $-1\%$  change of  $a_0$  and  $b_0$  at  $T_{\text{IM}}$  [36]. The  $\text{Ca}_2\text{RuO}_4$  samples often cleave upon warming and, more frequently, shatter in several pieces upon cooling [5]. This is naturally understood as due to the material fragility to expansion, which occurs in the out-of-plane direction upon warming and in-plane upon cooling. Consequently, we need to use multiple samples for our study (Fig. S3 [35]). Since the values of  $T_{\text{IM}}$  and  $T_{\text{MI}}$  are slightly different for each sample, we consider them as a range that we indicate with shaded regions in Fig. 1(b) and throughout this paper ( $T_{\text{IM}} = 85\text{--}100^\circ\text{C}$  in blue,  $T_{\text{MI}} = 65\text{--}80^\circ\text{C}$  in orange). These sample-to-sample variations can be due to slight differences in chemical stoichiometry, in the amount of microcracks, or in strain possibly caused by the gluing on the holder.

## B. Temperature-driven MIT

We now perform thermal imaging on  $\text{Ca}_2\text{RuO}_4$  during a warming-and-cooling ramp without any supplied current ( $I = 0$ ). The representative thermal images in Fig. 2(a) show that the raw IR reading  $T_{\text{raw}}$  is rather homogeneous over the sample surface. To measure the appropriate IR temperature,  $T_{\text{raw}}$  needs to be calibrated according to the emissivity of  $\text{Ca}_2\text{RuO}_4$ . To perform this calibration, we exploit the fact that in these conditions the sample is in thermal equilibrium with  $T_{\text{sm}}$ . We thus extract in Fig. 2(b) the dependence of  $T_{\text{raw}}$ , averaged over the sample surface, on  $T_{\text{sm}}$ . Upon warming,  $T_{\text{raw}}$  shows a sharp drop at  $T_{\text{IM}}$  when the sample becomes metallic. This drop is due to the decreased thermal emissivity of  $\text{Ca}_2\text{RuO}_4$  in the metallic phase, in accordance with its increased reflectivity [23]. Upon cooling,  $T_{\text{raw}}$  rises sharply at  $T_{\text{MI}}$  when the sample turns insulating, and it goes back to the previous curve.

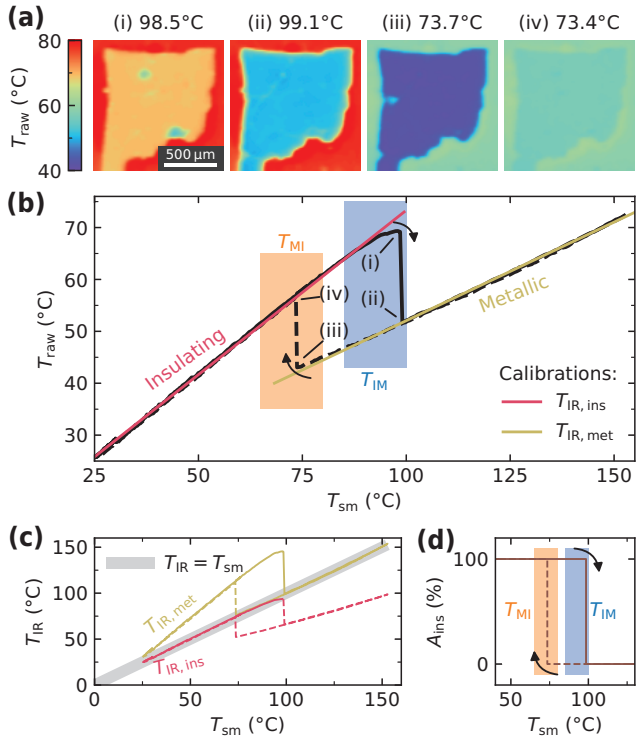


FIG. 2. Thermal imaging of the temperature-driven MIT in  $\text{Ca}_2\text{RuO}_4$  with  $I = 0$ . (a) Thermal images taken at different values of  $T_{\text{sm}}$ , as indicated (sample no. 2, pristine state, no electrical leads). Images (i) and (ii) show the insulator-to-metal transition upon warming, while images (iii) and (iv) show the metal-to-insulator transition upon cooling. (b) Raw reading of the IR camera  $T_{\text{raw}}$  averaged over the sample surface as a function of  $T_{\text{sm}}$ . The jumps in  $T_{\text{raw}}$  are due to the abrupt change in  $\text{Ca}_2\text{RuO}_4$  reflectivity at the MIT. Two linear regressions are used to separately calibrate  $T_{\text{IR}}$  for the insulating (red) and metallic (gold) phases. (c) IR temperature calculated from  $T_{\text{raw}}$  by using the two calibrations obtained in (b). Overlap with the gray line shows that the calibration  $T_{\text{IR, ins}}$  ( $T_{\text{IR, met}}$ ) is valid only when the sample is in the insulating (metallic) phase. (d) Percentage of insulating area  $A_{\text{ins}}$  as a function of temperature estimated by making use of the emissivity change. In this temperature-driven MIT, the whole sample changes phase at the same time.

The observed experimental behavior prompts for two different emissivity calibrations for the two phases. These are obtained by performing a linear regression for the insulating ( $T_{\text{IR, ins}}$ , red line) and for the metallic ( $T_{\text{IR, met}}$ , gold line) phases separately. We note that the regressions have some deviation from the experimental data, especially in the insulating phase close to  $T_{\text{IM}}$ . Furthermore, there are two additional sources of error that affect our calibration: the thermal contribution due to areas surrounding the sample, and sample-to-sample variations (Fig. S4 [35]). For these reasons, we estimate an uncertainty of about  $\pm 10^\circ\text{C}$  on the absolute temperature value provided by the calibrations. Since the same calibrations are used throughout this work, this error is of systematic character and it does not affect our findings. We comment that a smaller error on  $T_{\text{IR}}$  has been previously achieved by coating the sample with a blackbody insulating paste [18]. Nevertheless, our experimental configuration has the important advantage

of allowing direct imaging of metallic and insulating areas, as discussed in the following.

We use the obtained calibrations to convert  $T_{\text{raw}}$  into the appropriate IR temperature for the insulating and metallic phases in Fig. 2(c). As a reference, we also plot  $T_{\text{IR}} = T_{\text{sm}}$  (thick gray line), which is the result expected from an ideal calibration. Figure 2(c) shows that  $T_{\text{IR, ins}}$  has a good overlap with the gray line as long as the sample is in the insulating phase. In the metallic state, instead,  $T_{\text{IR, ins}}$  is significantly lower than the effective sample temperature, whereas  $T_{\text{IR, met}}$  overlaps the gray line.

The large change in emissivity at the MIT allows us to map the local distribution of metallic and insulating phases. Areas turning from insulating to metallic, in fact, suddenly appear darker in our images. For the case of the temperature-driven MIT presented here, the whole sample changes phase at the same time, as shown by the images of Fig. 2(a). This is a direct consequence of the spatially homogeneous temperature distribution over the sample, which is brought above  $T_{\text{MI}}$  or below  $T_{\text{IM}}$  all at the same time. In addition, the single-crystal nature of the sample contributes to a simultaneous phase transition in the entire volume. For these reasons, the percentage of insulating area  $A_{\text{ins}}$  as a function of temperature has a step-like trend [Fig. 2(d)]. As shown by the overlap with the orange and blue shaded areas,  $A_{\text{ins}}$  has a hysteresis compatible with the transport data of Fig. 1(b).

### C. Current-driven MIT

We now investigate how the electric current can drive the MIT in  $\text{Ca}_2\text{RuO}_4$ . For this measurement, we fix the Peltier-stage temperature to  $25^\circ\text{C}$  in air environment and drive the sample with a constant current source. We use a two-probe configuration in order to measure the voltage and power supplied to the whole sample. As shown in Fig. 3(a), the voltage-current characteristics has an initial linear trend, peaks at about 20 mA, and then evolves into a negative differential resistance. We observed a similar behavior also when driving the sample with a voltage source or a voltage divider (Fig. S5 [35]). This voltage-current characteristics is consistent with that observed in several previous experiments on  $\text{Ca}_2\text{RuO}_4$  under current flow [14, 17, 18, 20, 23, 24]. With increasing current, the supplied electrical power increases [Fig. 3(b)]. Consequently, both  $T_{\text{sm}}$  and  $T_{\text{h}}$  detect a small temperature increase of a few degrees [Fig. 3(c)]. At the same time, however, the actual sample temperature increases to a much larger extent:  $T_{\text{IR, ins}}$  shows a raise of several tens of  $^\circ\text{C}$  as measured by the IR camera in Fig. 3(e). This indicates that the temperature sensors placed on the sample holder largely underestimate the actual temperature of  $\text{Ca}_2\text{RuO}_4$  which is heated up by the direct current, as also reported by a recent study by Fürsich *et al.* [24]. This observation emphasizes the need for monitoring the local sample temperature as allowed by our imaging technique.

The temperature distribution over the sample surface is approximately homogeneous, apart from slightly hotter regions near the contacts, probably due to the higher current density dictated by the sample geometry. The low-resistance gold pads used for the electrical contacts guarantee a small power dissipation due to contact resistance (Fig. S2 [35]). In another

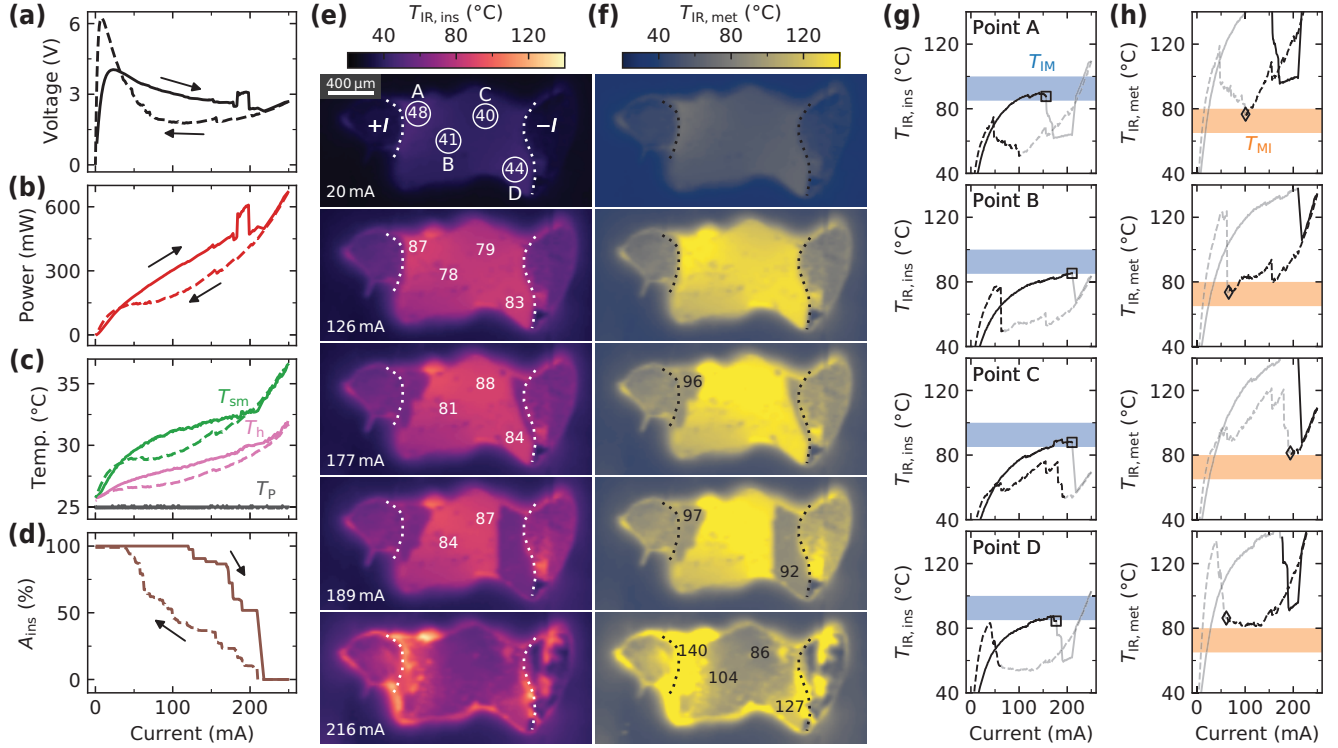


FIG. 3. Current-driven MIT in  $\text{Ca}_2\text{RuO}_4$ . (a) Voltage-current characteristics measured in a two-probe configuration and (b) corresponding electrical power (sample no. 3). (c) Temperature measured by the sample-monitor and holder sensors at a fixed  $T_p = 25^\circ\text{C}$ . (d) Percentage of insulating area extracted from the thermal images. (e) Thermal images with insulating and (f) metallic calibration. The temperature value of points A–D is indicated by a number in the image corresponding to the appropriate state of the point. The current electrodes are indicated by  $\pm I$  and the dotted lines. (g) Current dependence of the IR temperature obtained with the insulating and (h) metallic calibration for the points indicated by the circles in (e).

experimental configuration where the sample has a weaker thermal coupling with the cooling stage, we observe a Peltier effect at metal– $\text{Ca}_2\text{RuO}_4$  interfaces, which produces a higher temperature at the negative current electrode (Fig. S6 [35]). This Peltier effect and its sign are consistent with previous experimental and theoretical reports both on  $\text{Ca}_2\text{RuO}_4$  [23,40] and  $\text{VO}_2$  [41]. In the data presented here, Peltier effects are negligible due to the strong thermal coupling between the sample and the holder.

Upon increasing current, the metallic phase nucleates simultaneously at both current electrodes, from which it expands starting from the hotter regions close to the contacts [see the darker areas appearing in the third panel from the top in Fig. 3(e)]. We comment that in similar conditions nanoscale stripes at the phase front were reported by Zhang *et al.* [23], but we cannot resolve them with the present technique. The change in thermal emissivity gives us the unique possibility of extracting from the images  $A_{ins}$  [Fig. 3(d)], which progressively decreases with increasing current as the sample becomes more metallic. We comment that even though  $A_{ins}$  is estimated from the sample surface, we ensured a homogeneous current flow along the sample thickness by attaching the electrical leads covering the sample sides and using thin samples of single-crystal nature. For these reasons, we expect  $A_{ins}$  to extend to most of the cross

section for pristine samples (i.e., in the absence of severe cracks).

The appropriate temperature of metallic areas is provided by the calibration  $T_{IR,met}$  shown in Fig. 3(f). Once the metallic phase appears, the resistivity is locally reduced resulting in a lower local dissipation of electrical power. This effect is expected to produce a local cooling, but in reality it leads to complex rearrangements of the effective current path, sometimes causing a local switch back to the insulating phase, or to repeated insulating/metallic switches. In most cases, however, the MIT hysteresis prevents the newly formed metallic areas from going back to the insulating state. Due to the  $\pm 10^\circ\text{C}$  uncertainty in our temperature calibrations, we cannot experimentally assess whether regions turning metallic experience a local cooling.

For  $I > 215$  mA the entire sample is in the metallic state. Upon decreasing current, the sample cools down and progressively goes back to the insulating state. At this point, the curves in Figs. 3(a)–3(d) show a hysteresis that can be due to various effects. First, there is the intrinsic hysteresis of the MIT as discussed in Fig. 1(b). Second, when the current is decreased from the maximum value, the sample is in the less resistive metallic state so that the voltage, power, and sensor temperatures also have lower values. Third, the current-induced MIT leads to the irreversible formation of cracks and



defects, as will be discussed in the following subsection. The presence of this irreversible effect is also evidenced by the fact that once the sample goes back to the insulating state at low current, the peak in the  $V-I$  curve [Fig. 3(a)] occurs at a higher voltage value and the sample has a higher resistivity.

Our imaging technique allows us to extract the local temperature of some representative points [A–D in Fig. 3(e)] as a function of applied current. We report in Figs. 3(e) and 3(f) the local temperature of these points using the insulating and metallic calibrations, respectively. We use a solid line for the increasing-current ramp and a dashed line for the decreasing current. Data with the calibration matching the appropriate phase are shown in black, while the rest are in shaded gray. The curves in Fig. 3(g) show the local temperature increase due to the increasing current up to the point where the insulator-to-metal transition occurs (open squares). The opposite phase transition (metal-to-insulator) can be observed in Fig. 3(h) upon decreasing current, as indicated by the open diamonds. We note that the square and diamond markers lie, within our experimental resolution, within the ranges of  $T_{IM}$  and  $T_{MI}$ , respectively. This indicates that the current-driven MIT is triggered whenever the local temperature of an area goes above  $T_{IM}$  or below  $T_{MI}$ . The experimental setup used in the present work does not allow us to detect additional nonthermal effects induced by the electrical current, which may have caused changes in  $T_{IM}$  and  $T_{MI}$  smaller than our uncertainty of  $\pm 10^\circ\text{C}$ .

Finally, we comment on the temperature gradients observed in the insulating and metallic phases. With increasing current up to the fourth row of Figs. 3(e) and 3(f) ( $I = 189\text{ mA}$ ), the temperature of the representative points is rather homogeneous both in the insulating ( $84, 87^\circ\text{C}$ ) and in the metallic ( $97, 92^\circ\text{C}$ ) phases. With higher currents (fifth row at  $216\text{ mA}$ ), the sudden switch of a large sample portion to the metallic phase leads to the formation of several cracks. We anticipate a larger resistance in the proximity of these cracks, causing a large local dissipation of power (hot spots), and thus a larger temperature inhomogeneity ( $140, 104, 86, 127^\circ\text{C}$ ). This inhomogeneity has hence an extrinsic origin.

#### D. Current-driven MIT in the presence of cracks and defects

To study how the formation of cracks and defects affects the current-driven MIT, we perform multiple current cycles that bring the sample to the metallic state and then back to the insulating state. We fix the thermal bath at  $T_P = 25^\circ\text{C}$  and increase the current up to a few mA more than what is required to switch the entire sample to the metallic phase; we then decrease it back to zero and start the next cycle (rates of  $0.5\text{ mA s}^{-1}$ ). We show in Figs. 4(a) and 4(b) the two-probe  $V-I$  characteristics and value of  $A_{ins}$  measured during nine consecutive cycles. At each cycle, the voltage peak increases and shifts to lower currents [triangles in Fig. 4(a)] and to lower corresponding current densities [ $j_{peak}$  in Fig. 4(c)]. Concomitantly, the entire sample turns metallic at a lower current [stars in Fig. 4(b)] and current density [ $j_{all-met}$  in Fig. 4(c)]. This occurs because a higher power is dissipated in the sample due to its increased resistance. The drop of more than one order of magnitude in  $j_{all-met}$  indicates large and irreversible changes in the sample properties, consistent with the previous

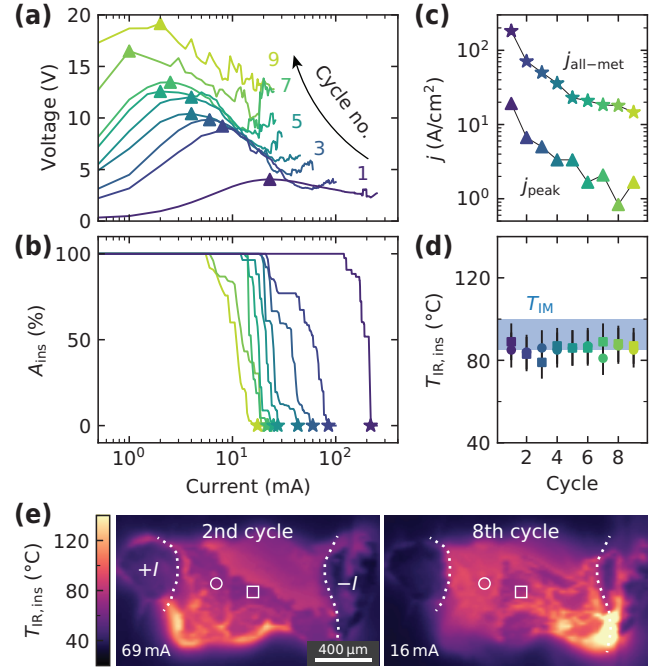


FIG. 4. Multiple cycles of current-driven MIT. (a) Current dependence of the two-probe voltage and (b) percentage of insulating area for the different increasing-current sweeps (sample no. 3). (c) Current density at the voltage peak (triangles) and when the sample becomes all metallic (stars) as a function of cycle number. (d) IR temperature at which the regions indicated by the circle and the square in (e) turn metallic as a function of cycle number. (e) Representative thermal images at different current cycles during the increasing ramp. The presence of a hot spot in the bottom left (right) corner during the second (eighth) current cycle drives the formation of the metallic phase from the left (right) corner.

observation of crack formation at similar current values [42]. These macroscopic defects can be clearly observed under the optical microscope (Fig. S7 [35]).

The formation of cracks and defects strongly affects the temperature distribution over the sample surface, leading to the formation of hot spots responsible for higher power dissipation, as can be seen in the images of Fig. 4(e). It is clear that, despite the comparable values of  $A_{ins}$ , the presence of hot spots in the lower left (right) corner during the second (eighth) cycle drives a preferential metallic phase formation from the left (right) electrode. We select two representative regions, indicated by the circle and square in Fig. 4(e), and report in Fig. 4(d) the values of  $T_{IR,ins}$  at which they become metallic at each current cycle. The values of  $T_{IR,ins}$  are rather constant and in good agreement with the temperature range of  $T_{IM}$  [shaded blue area in Fig. 4(d)], even if the insulator-to-metal transition in these regions occurs for very different current densities at each cycle. These data are a further indication that, in our experimental conditions and irrespective of the sample state, the main trigger for the current-induced MIT is the local sample temperature.

### III. CONCLUSIONS

To conclude, we were able to observe the current-induced formation of metallic and insulating regions in  $\text{Ca}_2\text{RuO}_4$  by means of thermal IR imaging. Our data show that while the insulator-to-metal transition can occur over a broad range of current densities, it is always triggered whenever the local sample temperature exceeds  $T_{\text{MI}}$ . Within our resolution, the local  $T_{\text{MI}}$  is the same regardless of whether the MIT is triggered by temperature, by current, or by current in the presence of macroscopic cracks and defects. In our experimental conditions we find that direct heating of the sample due to the Joule effect is much larger than what is detected by thermometers that monitor the sample holder temperature. These findings uncover an important balance of local heating, phase coexistence, and microscale inhomogeneity in  $\text{Ca}_2\text{RuO}_4$  that is of the utmost importance when performing measurements with applied current. These effects can potentially have a large

influence also on macroscopic measurements, which may average the contribution of coexisting metallic and insulating regions. The present work sets an important basis to perform future experiments to uncover current-induced nonequilibrium steady-state effects.

### ACKNOWLEDGMENTS

We thank G. Chiriacò, K. Fürsich, M. Liu, N. Manca, A. Millis, H. Narita, R. Okazaki, D. Ootsuki, I. Terasaki, T. Yoshida, and A. Vecchione for fruitful discussions. This work was supported by Japan Society for the Promotion of Science (JSPS) Grants-in-Aid KAKENHI No. JP26247060, No. JP15H05852, No. JP15K21717, and No. JP17H06136, as well as by JSPS Core-to-Core program. G.M. acknowledges support from the Dutch Research Council (NWO) through a Rubicon Grant No. 019.183EN.031.

- 
- [1] B. Keimer and J. Moore, *Nat. Phys.* **13**, 1045 (2017).
  - [2] D. Basov, R. Averitt, and D. Hsieh, *Nat. Mater.* **16**, 1077(R) (2017).
  - [3] S. Nakatsuji, S.-i. Ikeda, and Y. Maeno, *J. Phys. Soc. Jpn.* **66**, 1868 (1997).
  - [4] M. Braden, G. André, S. Nakatsuji, and Y. Maeno, *Phys. Rev. B* **58**, 847 (1998).
  - [5] C. S. Alexander, G. Cao, V. Dobrosavljevic, S. McCall, J. E. Crow, E. Lochner, and R. P. Guertin, *Phys. Rev. B* **60**, R8422 (1999).
  - [6] I. Zegkinoglou, J. Stremper, C. S. Nelson, J. P. Hill, J. Chakhalian, C. Bernhard, J. C. Lang, G. Srajer, H. Fukazawa, S. Nakatsuji, Y. Maeno, and B. Keimer, *Phys. Rev. Lett.* **95**, 136401 (2005).
  - [7] A. Jain, M. Krautloher, J. Porras, G. Ryu, D. Chen, D. Abernathy, J. Park, A. Ivanov, J. Chaloupka, G. Khaliullin *et al.*, *Nat. Phys.* **13**, 633 (2017).
  - [8] G. Cao, S. McCall, V. Dobrosavljevic, C. S. Alexander, J. E. Crow, and R. P. Guertin, *Phys. Rev. B* **61**, R5053(R) (2000).
  - [9] J. Carlo, T. Goko, I. Gat-Malureanu, P. Russo, A. Savici, A. Aczel, G. MacDougall, J. Rodriguez, T. Williams, G. Luke *et al.*, *Nat. Mater.* **11**, 323 (2012).
  - [10] F. Nakamura, T. Goko, M. Ito, T. Fujita, S. Nakatsuji, H. Fukazawa, Y. Maeno, P. Alireza, D. Forsythe, and S. R. Julian, *Phys. Rev. B* **65**, 220402(R) (2002).
  - [11] P. Steffens, O. Friedt, P. Alireza, W. G. Marshall, W. Schmidt, F. Nakamura, S. Nakatsuji, Y. Maeno, R. Lengsdorf, M. M. Abd-Elmeguid *et al.*, *Phys. Rev. B* **72**, 094104 (2005).
  - [12] P. L. Alireza, F. Nakamura, S. K. Goh, Y. Maeno, S. Nakatsuji, Y. T. C. Ko, M. Sutherland, S. Julian, and G. G. Lonzarich, *J. Phys.: Condens. Matter* **22**, 052202 (2010).
  - [13] L. Miao, W. Zhang, P. Silwal, X. Zhou, I. Stern, T. Liu, J. Peng, J. Hu, D. H. Kim, and Z. Q. Mao, *Phys. Rev. B* **88**, 115102 (2013).
  - [14] N. Shukla, M. Jerry, H. Nair, M. Barth, D. G. Schlom, and S. Datta, in *2016 74th Annual Device Research Conference (DRC)* (IEEE, Piscataway, NJ, 2016), pp. 1–2.
  - [15] C. Dietl, S. Sinha, G. Christiani, Y. Khaydukov, T. Keller, D. Putzky, S. Ibrahimkuty, P. Wochner, G. Logvenov, P. van Aken *et al.*, *Appl. Phys. Lett.* **112**, 031902 (2018).
  - [16] S. Riccò, M. Kim, A. Tamai, S. M. Walker, F. Y. Bruno, I. Cucchi, E. Cappelli, C. Besnard, T. K. Kim, P. Dudin *et al.*, *Nat. Commun.* **9**, 4535 (2018).
  - [17] F. Nakamura, M. Sakaki, Y. Yamanaka, S. Tamaru, T. Suzuki, and Y. Maeno, *Sci. Rep.* **3**, 2536 (2013).
  - [18] R. Okazaki, Y. Nishina, Y. Yasui, F. Nakamura, T. Suzuki, and I. Terasaki, *J. Phys. Soc. Jpn.* **82**, 103702 (2013).
  - [19] J. Bertinshaw, N. Gurung, P. Jorba, H. Liu, M. Schmid, D. T. Mantadakis, M. Daghofer, M. Krautloher, A. Jain, G. H. Ryu, O. Fabelo, P. Hansmann, G. Khaliullin, C. Pfleiderer, B. Keimer, and B. J. Kim, *Phys. Rev. Lett.* **123**, 137204 (2019).
  - [20] C. Cirillo, V. Granata, G. Avallone, R. Fittipaldi, C. Attanasio, A. Avella, and A. Vecchione, *Phys. Rev. B* **100**, 235142 (2019).
  - [21] H. Zhao, B. Hu, F. Ye, C. Hoffmann, I. Kimchi, and G. Cao, *Phys. Rev. B* **100**, 241104(R) (2019).
  - [22] R. Okazaki, K. Kobayashi, R. Kumai, H. Nakao, Y. Murakami, F. Nakamura, H. Taniguchi, and I. Terasaki, *J. Phys. Soc. Jpn.* **89**, 044710 (2020).
  - [23] J. Zhang, A. S. McLeod, Q. Han, X. Chen, H. A. Bechtel, Z. Yao, S. N. Gilbert Corder, T. Ciavatti, T. H. Tao, M. Aronson, G. L. Carr, M. C. Martin, C. Sow, S. Yonezawa, F. Nakamura, I. Terasaki, D. N. Basov, A. J. Millis, Y. Maeno, and M. Liu, *Phys. Rev. X* **9**, 011032 (2019).
  - [24] K. Fürsich, J. Bertinshaw, P. Butler, M. Krautloher, M. Minola, and B. Keimer, *Phys. Rev. B* **100**, 081101(R) (2019).
  - [25] K. Jenni, F. Wirth, K. Dietrich, L. Berger, Y. Sidis, S. Kunkemöller, C. P. Grams, D. I. Khomskii, J. Hemberger, and M. Braden, *Phys. Rev. Materials* **4**, 085001 (2020).
  - [26] C. Sow, S. Yonezawa, S. Kitamura, T. Oka, K. Kuroki, F. Nakamura, and Y. Maeno, *Science* **358**, 1084 (2017).
  - [27] C. Sow, R. Numasaki, G. Mattoni, S. Yonezawa, N. Kikugawa, S. Uji, and Y. Maeno, *Phys. Rev. Lett.* **122**, 196602 (2019).
  - [28] C. Sow, S. Yonezawa, S. Kitamura, T. Oka, K. Kuroki, F. Nakamura, and Y. Maeno, *Science* **368**, 376 (2020).
  - [29] C. Sow, R. Numasaki, G. Mattoni, S. Yonezawa, N. Kikugawa, S. Uji, and Y. Maeno, *Phys. Rev. Lett.* **124**, 169902(E) (2020).

- [30] G. Mattoni, S. Yonezawa, and Y. Maeno, *Appl. Phys. Lett.* **116**, 172405 (2020).
- [31] A. A. Fursina, R. G. S. Sofin, I. V. Shvets, and D. Natelson, *Phys. Rev. B* **79**, 245131 (2009).
- [32] A. Zimmers, L. Aigouy, M. Mortier, A. Sharoni, S. Wang, K. G. West, J. G. Ramirez, and I. K. Schuller, *Phys. Rev. Lett.* **110**, 056601 (2013).
- [33] N. Shukla, T. Joshi, S. Dasgupta, P. Borisov, D. Lederman, and S. Datta, *Appl. Phys. Lett.* **105**, 012108 (2014).
- [34] G. Mattoni, N. Manca, M. Hadjimichael, P. Zubko, A. J. H. van der Torren, C. Yin, S. Catalano, M. Gibert, F. Maccherozzi, Y. Liu, S. S. Dhesi, and A. D. Caviglia, *Phys. Rev. Materials* **2**, 085002 (2018).
- [35] See Supplemental Material at <http://link.aps.org/supplemental/10.1103/PhysRevMaterials.4.114414> for detailed structural characterization of our  $\text{Ca}_2\text{RuO}_4$  crystals, details on the electrical contacts, a summary of the main samples used for this study, details on the thermal emissivity calibration, different configurations used to measure voltage-current characteristics, current-induced Peltier heating, and optical observation of cracks.
- [36] O. Friedt, M. Braden, G. André, P. Adelman, S. Nakatsuji, and Y. Maeno, *Phys. Rev. B* **63**, 174432 (2001).
- [37] F. Morin, *Phys. Rev. Lett.* **3**, 34 (1959).
- [38] G. Mattoni, P. Zubko, F. Maccherozzi, A. J. van der Torren, D. B. Boltje, M. Hadjimichael, N. Manca, S. Catalano, M. Gibert, Y. Liu *et al.*, *Nat. Commun.* **7**, 13141 (2016).
- [39] D. Fobes, E. Vehstedt, J. Peng, G. Wang, T. Liu, and Z. Mao, *J. Appl. Phys.* **111**, 083709 (2012).
- [40] G. Chiriacò and A. J. Millis, *Phys. Rev. B* **102**, 085116 (2020).
- [41] T. Favaloro, J. Suh, B. Vermeersch, K. Liu, Y. Gu, L.-Q. Chen, K. X. Wang, J. Wu, and A. Shakouri, *Nano Lett.* **14**, 2394 (2014).
- [42] M. Sakaki, N. Nakajima, F. Nakamura, Y. Tezuka, and T. Suzuki, *J. Phys. Soc. Jpn.* **82**, 093707 (2013).